Revealing substitution mechanism in Eu^{3+}:$CaMoO_4$ and Eu^{3+},Na^{+}:$CaMoO_4$ phosphors.

Ana Isabel Becerro,[*a] Mathieu Allix,[*b] Mariano Laguna,[a] Daniel González-Mancebo,[a] Cecile Genevois,[b] Alfonso Caballero,[a] Gabriel Lozano,[a] Nuria O. Núñez,[a] Manuel Ocaña[a]

[a] Instituto de Ciencia de Materiales de Sevilla (CSIC-US), c/Américo Vespucio, 49, 41092 Seville, Spain

[b] CNRS, CEMHTI UPR3079, Universite Orléans, F-45071 Orléans, France.

Abstract

Eu^{3+}-doped calcium molybdate is an excellent phosphor for lighting and display devices due to the very intense pure red emission after UV excitation. It has been reported in the literature that the $CaMoO_4$ unit cell volume expands after Eu^{3+} doping, in spite of the smaller Eu^{3+} ionic radius compared with Ca^{2+}. Likewise, several studies found that the emission intensity of the phosphor could be improved by codoping with alkaline ions like Li^{+}, Na^{+} or K^{+}. None of these studies correlated the apparent volume expansion and luminescence enhancement with the crystal structural details. This paper analyses the aliovalent substitution mechanism and crystal structure of Eu^{3+}:$CaMoO_4$ and Eu^{3+},Na^{+}:$CaMoO_4$ phosphors using complementary techniques like Raman spectroscopy, EXAFS and SPD. We found that the substitution mechanism was different for both systems, with Ca site vacancies forming in the Eu^{3+}:$CaMoO_4$ phosphors and leading to $Ca_{1-3x}Eu_{2x}\square_xMoO_4$ compositions, while the Eu^{3+},Na^{+}:$CaMoO_4$ phosphors formed $Ca_{1-2x}Eu_xNa_xMoO_4$. SPD showed that the cell volume expansion observed with increasing Eu^{3+} content is related to the increase of the Mo-O bond distance due to the higher electronegativity of Eu^{3+} compared with Ca^{2+}. Finally, it was shown that the luminescence properties, i.e. lifetime values and quantum yields (the latter reported here for the first time), do not depend on the presence of monovalent ions in the crystal structure but, exclusively, on the Eu^{3+} content of the phosphor. The integral and detailed analysis of the materials presented in this paper, ranging from crystal structure to luminescent properties including elemental composition allows a full draw of the structure-properties relationship that had never been addressed before for $CaMoO_4$-based phopshors.

[*] Corresponding authors: anieto@icmse.csic.es (Ana Isabel Becerro) and mathieu.allix@cnrs-orleans.fr (Mathieu Allix)

1. INTRODUCTION

Calcium molybdate ($CaMoO_4$) is an important photoluminescent material with potential applications in scintillators,[1] photocatalysis,[2] etc. $CaMoO_4$ emits light in the blue-green region of the electromagnetic spectrum after excitation with UV light.[3] $CaMoO_4$ crystallizes in the scheelite structure (tetragonal, space group $I4_1/a$), with molybdenum atoms surrounded by four equivalent oxygen (T_d symmetry) and Ca atoms coordinated to eight oxygen atoms.[4] Each CaO_8 polyhedron shares corners with eight adjacent MoO_4 tetrahedra. A schematic structure of $CaMoO_4$ scheelite is provided in **Figure 1**. $CaMoO_4$ is also an interesting host matrix for lanthanide-doped phosphor materials that produces narrow spectral emission lines due to intra *4f* electronic transitions. Interestingly, the $[MoO_4]^{2-}$ unit can absorb UV light with a high cross-section and excite the doping lanthanide ion through the so-called energy transfer process, which notably enhances the emission intensity of the lanthanide ions. Among the latter, Eu^{3+} ions are easily substituted for Ca^{2+} into $CaMoO_4$ due to the similar ionic radii of Ca^{2+} (1.12 Å in VIII coordination) and Eu^{3+} (1.066 Å in VIII coordination). The excellent luminescent properties together with the high chemical and thermal stability of the $CaMoO_4:Eu^{3+}$ phosphor has attracted a lot of attention in the last decade. Photoluminescence properties of $CaMoO_4:Eu^{3+}$ have been extensively studied in bulk samples,[5,6,7,8] microparticles[3,9,10,11] and different types of nanoparticles.[12,13,14,15] However, very little attention has been paid to the substitution mechanism and crystal structure of $Eu^{3+}:CaMoO_4$ phosphors. In our recent paper on the photoluminescence of peanut-like $CaMoO_4:1\%Eu^{3+}$ architectures, we found that the unit cell parameters of the Eu^{3+}-doped sample were slightly higher than those of the undoped material, in spite of the smaller ionic radius of Eu^{3+} compared with Ca^{2+} in eight-fold coordination.[11] Some other authors have also noticed such a volume increase with Eu^{3+} doping in $Eu^{3+}:CaMoO_4$ phosphors,[6,9,16] although none of them has carried out a deep structural study to envisage the substitution mechanism and the resulting crystal structure. Likewise, several authors have reported that the emission of $CaMoO_4:Eu^{3+}$ was enhanced by co-doping with Na^+, Li^+ or K^+.[5,17] However, none of these studies correlated the apparent luminescence enhancement with the actual elemental composition of the samples and the crystal structure derived from the substitution mechanism of Ca^{2+} by Eu^{3+}, Na^+, Li^+ or K^+.

In this paper, we study the aliovalent substitution mechanism and the crystal structure of $Eu^{3+}:CaMoO_4$ and $Eu^{3+},Na^+:CaMoO_4$ phosphors. From a structural point of view, there should be a charge balance mechanism when substituting one Ca^{2+} ion by one Eu^{3+} ion in $Eu^{3+}:CaMoO_4$. Two possible mechanisms to maintain charge neutrality in these materials with aliovalent ionic substitution include *i)* Ca-site vacancies ($3Ca_{Ca} \rightarrow 2Eu_{Ca}^{\cdot} + V_{Ca}^{''}$) forming $Ca_{1-3x}Eu_{2x}\square_xMoO_4$ (where □ represents a vacant Ca site) or *ii)* interstitial oxygen atoms ($2Ca_{Ca} \rightarrow 2Eu_{Ca}^{\cdot} + O_i^{''}$) forming $Ca_{1-x}Eu_xMoO_{4+x/2}$. A third possible mechanism to maintain electrical neutrality involves the co-doping of the $CaMoO_4$ scheelite structure with Eu^{3+} and an alkaline cation (A^+) like Na^+, Li^+ or K^+ to form $Ca_{1-2x}Eu_xA_xMoO_4$, as reported in the case of calcium wolframate.[18] In order to figure out the substitution mechanism, two series of samples (with and without sodium in the reaction medium) were synthesized using a liquid-based method followed by calcination. The nominal

Eu/(Eu+Ca) mol % ratio was varied from 0 to 50% in both series. Elemental analyses and Raman spectroscopy were used to envisage the ionic substitution mechanism, while synchrotron powder diffraction and EXAFS were employed to analyze the resulting crystal structures and ascertain the substitution mechanism. Finally, the influence of Eu^{3+}, Na^{+} and vacancy contents on the photoluminescence emission intensity were examined in detail while lifetime and quantum yield measurements were carried out to analyze the effects of the substitution mechanism.

2. EXPERIMENTAL SECTION

2.1. Reagents

Calcium nitrate ($Ca(NO_3)_2 \cdot 4H_2O$, Aldrich, 99%), europium nitrate ($Eu(NO_3)_3 \cdot 5H_2O$, Aldrich, 99.9%), sodium molybdate (Na_2MoO_4, Aldrich, ≥98%) and ammonium molybdate ($(NH_4)_2MoO_4$, Aldrich, ≥98%) were selected as precursors. Glycerol (Aldrich, ≥99.5%) and miliQ water were used as solvent. All chemicals were used as received.

2.2. Synthesis method

Eu^{3+}:$CaMoO_4$ samples containing different amounts of Eu^{3+} were synthesized using the method reported by Laguna et al.[11] followed by calcination at 900 ºC for 5 hours. Briefly, the method consisted of the aging, at 120 ºC for 20 hours, a glycerol/H_2O (4/1 volumetric ratio) solution containing calcium and europium nitrates and $(NH_4)_2MoO_4$ (0.05 M). Different Eu contents, expressed as Eu/(Eu+Ca) molar ratio, were used (0%, 10%, 30% and 50%) while keeping constant (0.01 M) the Eu+Ca concentration in the solution. The resulting dispersions were centrifuged to remove the supernatants, washed with ethanol and dried at 60ºC. The white powders obtained were then calcined in alumina crucibles at 900ºC for 5 hours. Na_2MoO_4 was also used as Mo source to investigate the effect of Na^{+} on the structure of the obtained materials. All the other experimental parameters were constant with respect to the Na-free samples.

Samples synthesized from ammonium molybdate will thereafter be named AMo-*x* while those synthesized from sodium molybdate will be called NaMo-*x*, where *x* indicates the nominal Eu/(Ca+Eu) molar ratio.

2.3. Characterization techniques

Elemental composition of the samples was analyzed by energy dispersive X-ray spectroscopy using an EDX Bruker X Flash Detector 4010 attached to a SEM microscope (FEGSEM, Hitachi S4800, 20 kVHitachi4800). The analyses were carried out on powder samples. An acquisition time as long as 10 minutes was used to record each spectrum, in order to obtain reliable quantitative results. EDS analyses were also performed at the TEM in order to confirm these results at the nanometer scale.

Laboratory X-ray diffraction patterns were recorded on a PANalytical X'Pert Pro diffractometer equipped with an X-Celerator detector. Data were collected over an angular range of 10 to 70 º2θ using 0.05º steps.

Raman spectra (200–2000 cm^{-1}) were recorded on a Lab-RAM Horiba Jobin Yvon spectrometer equipped with a CCD detector and a diode-pumped solid state laser (785 nm) at 5 mW. All samples were analyzed during 100 s of exposure time using a 100 μm aperture hole.

High-intensity and high-resolution synchrotron powder diffraction (SPD) data were carried out on the 11BM beamline at the Advanced Photon Source, Argonne National Laboratory, US. Data were collected at room temperature on a spinning sample (60 Hz) over the $0.5 - 50° 2\theta$ range with a 0.001° step using a $\lambda = 0.412708$ Å wavelength.

The X-ray absorption spectra (XAS spectra) were recorded at the BM25 beam line (SPLINE) of the ESRF synchrotron (Grenoble, France). The spectra were acquired at room temperature at the Mo K-edge (19.8-20.8 keV) and Eu L3-edge (6.8-7.8 keV) in transmission mode using self-supported wafers of the powder samples prepared using the optimum weight to maximize the signal-to-noise ratio in the ionization chambers (log I0/I1z1). Standard Mo and Fe foils were introduced for energy calibration of both edges after the second ionization chamber (I1) and measured simultaneously. The EXAFS region of the XAS spectra were mathematical extracted from the general XAS spectra, and the oscillations were Fourier transformed in the ranges 2.5-15.0 $Å^{-1}$ (Mo K-edge) and 3.0-11.0 $Å^{-1}$ (Eu L3-edge). Reference spectra for MoO_2, MoO_3, $(NH_4)_2MoO_4$ and Eu_2O_3 were recorded using commercial samples.

Excitation and emission spectra of the Eu^{3+}-containing samples were measured in a Horiba Jobin Yvon spectrofluorimeter (Fluorolog3). The samples were filling a hole (8 mm diameter) practiced in a methacrylate holder and cover with a quartz slide. This arrangement allows not only keeping an approximately constant amount of sample, but also preserving the geometry for reproducible luminescence measurements. The excitation/emission slits used to record the excitation and emission spectra were 0.6/1 nm and 1/0.6 nm, respectively. All spectra were recorded using 1 nm steps and they were corrected to account for the spectral response of the experimental setup. Eu^{3+} decay curves were collected in the same fluorimeter with a pulsed lamp at λ_{exc}= 270 nm while recording the luminescence decay at λ_{em}= 614 nm, associated to the $^5D_0$–$^7F_2$ transition of Eu^{3+}. The photoluminescence quantum yield (QY), defined as the ratio between photons emitted and absorbed, was determined by an absolute method. The measurements were carried out using a FLS100 Edinburgh fluorimeter equipped with an integrating sphere. Spectra were recorded at an excitation wavelength of 295 nm corresponding to the excitation band of the molybdate matrix. An emission wavelength of 614 nm was used, which corresponds to the most intense emission band of Eu^{3+}. The powder samples were deposited on a circular sample holder. A scattering plug made of the same material as the sphere was used as blank.

3. RESULTS AND DISCUSSION

3.1. Laboratory X-ray diffraction

The long-range order structure of the samples was analyzed by XRD. The XRD patterns of the samples synthesized from the ammonium molybdenum precursor (AMo-x samples) are shown in **Figure 2a**. All reflections in the pattern of the undoped material (AMo-0) could be indexed using the tetragonal $CaMoO_4$ scheelite structure (S.G. *$I4_1/a$,* PDF 00-029-0351). The patterns of the doped samples were very similar to each other and to the one of the undoped material, and showed exclusively reflections corresponding to the scheelite structure. Therefore, substitution of Ca^{2+} by Eu^{3+} did not cause any long-range order change in the scheelite structure. The reflections were however shifted towards lower 2θ angles with increasing Eu^{3+} content, as clearly observed in the inset of Figure 2a, which shows the 57.5 - 58.5 °2θ portion of the patterns. The observed shifting indicates an expansion of the unit cell volume, which is unexpected given the lower ionic radius of Eu^{3+} (1.066 Å in VIII coordination) compared with Ca^{2+} (1.12 Å in VIII coordination). Such a volume increase in Eu^{3+}:$CaMoO_4$ phosphors with increasing Eu^{3+} content was previously reported, although the origin of such behavior was never explained.[6,9,11,16] The XRD patterns of the samples synthesized from Na_2MO_4 (NaMo-x samples) are shown in **Figure 2b.** They exhibit a very similar behavior to the one described above for the AMo samples, showing exclusively scheelite reflections that shift to lower 2θ values with increasing Eu^{3+} content.

3.2. Elemental analyses

Elemental compositions of the samples synthesized from the ammonium molybdenum precursor (AMo-x samples) and from the sodium molybdenum precursor (NaMo-x samples) were obtained by EDX spectroscopy and are given in molar ratio with respect to Mo in **Table 1**. **Figure 3a** shows the occupation of the *A* site (Ca site in the pristine $CaMoO_4$ structure) calculated as Ca+Eu content in AMo samples and as Ca+Eu+Na content in NaMo samples. It can be observed that the *A* site is fully occupied in NaMo samples, i.e., all data points are close to the green line that represents full occupation (=1). However, the *A* site occupation in AMo samples decreases with increasing Eu^{3+} content, which is a clear indication of the existence of Ca vacancies in this case. **Figure 3b** represents the charge on the *A* site calculated on the basis of the Ca^{2+}, Eu^{3+} and Na^{+} contents of Table 1 for the samples in the AMo and NaMo series. Samples in both series show a charge value for the *A* site very close to 2 (green line), which indicates charge balance in all samples. Combination of data in Figures 3a and 3b supports a substitution mechanism in AMo samples consisting of the creation of Ca site vacancies forming $Ca_{1-3x}Eu_{2x}\square_xMoO_4$ *versus* the second possible mechanism suggested in the introduction section, which was based on the insertion of interstitial oxygen atoms. On the other hand, the substitution of Ca^{2+} by Eu^{3+} in NaMo samples does not seem to lead to the creation of Ca vacancies but the charge balance would be reached, in this case, by co-doping with Na^{+} ions to form $Ca_{1-2x}Eu_xNa_xMoO_4$ compositions. The formula unit calculated for each sample following the suggested substitution mechanisms is given on **Table 1**. Finally, the experimental Eu^{3+} content of each sample has been plotted in **Figure 3c** *versus* the nominal values for both series. The nominal values correspond to Eu contents based on the Eu/(Eu+Ca) molar ratios used in the synthesis (0, 10%, 30 and 50%, green line in the figure), assuming substitution of 1 mol of Ca^{2+} by 1 mol of Eu^{3+}. Observation of **Figure**

3c reveals that *i)* experimental values are lower than nominal ones (green line) in both series and *ii)* Eu^{3+} contents in NaMo samples are even lower than in AMo samples. As described above, the elemental composition data suggest a substitution of 3 moles of Ca^{2+} with 2 moles of Eu^{3+} in AMo samples, and the substitution of 2 moles of Ca^{2+} with 1 mol of Eu^{3+} in NaMo samples. In both cases, therefore, the experimental Eu^{3+} content is expected to be lower than the nominal one. Likewise, on the basis of the proposed substitution mechanisms, the Eu^{3+} content in NaMo samples is expected to be lower than in AMo samples, in good agreement with the data points in **Figure 3c**.

3.3. Raman spectroscopy

Figures 4a and 4b show the Raman spectra obtained for the samples in the AMo and NaMo systems. The spectra of the AMo-0 and NaMo-0 (pure $CaMoO_4$ matrix) are identical to each other and exhibit three sets of very narrow bands in the 900-750 cm^{-1}, 400-250 cm^{-1} and 250-100 cm^{-1} intervals. All of them can be assigned to the $CaMoO_4$ scheelite structure, which further confirms the phase purity of both samples.[19] The first group of bands, with maxima at 875, 844 and 790 cm^{-1}, are due to the stretching modes of Mo-O bonds in MoO_4 tetrahedra while the bending modes in such tetrahedra give rise to the second group of bands with maxima at 400, 388, 320 and 264 cm^{-1}. The third group of bands located at wavenumbers < 250 cm^{-1}, with maxima at 202, 187, 140 and 108 cm^{-1}, is composed of translational and rotational bands associated with the interactions between the Ca^{2+} cation and the MoO_4 tetrahedra.[19]

Increasing Eu^{3+} content in the AMo series gave rise to the broadening of all bands in the spectra and to the appearance of additional absorption bands in the Mo-O stretching modes region, with maxima at 896, 921 and 938 cm^{-1}, whose intensity significantly increased with increasing Eu^{3+} content. Similar bands were observed in the analogous Gd:$CdMoO_4$ system and were assigned to distorted MoO_4 tetrahedra caused by cationic vacancies in the neighboring $(Cd,Gd)O_8$ polyhedra.[20] In our case, these bands could therefore be due to the distortion of MoO_4 tetrahedra caused by cationic vacancies in $(Ca,Eu)O_8$ polyhedra. In addition, a clear shift of the bands associated with the interactions between the Ca^{2+} cation and the MoO_4 tetrahedra towards lower frequency values can be observed with increasing Eu^{3+} content (magnified region plotted as inset in Figure 4a), which suggests the presence of Eu^{3+} in the neighboring polyhedra. All these observations agree well with the substitution mechanism proposed in the previous section, where Ca^{2+} is replaced with Eu^{3+} ions and vacancies.

The Raman spectra in the NaMo series also show an additional band in the region corresponding to the stretching modes of Mo-O bonds, although with much lower intensity when compared with the AMo series. This is in agreement with much less distorted MoO_4 tetrahedra as compared with the AMo series, the distortion being likely due to the presence of Na^+ in the neighboring CaO_8 polyhedra. Likewise, a similar shift of the bands associated with the interactions between the Ca^{2+} cation and the MoO_4 tetrahedra can also be observed in this series (magnified region plotted as inset in Figure 4b), which indicates the replacement of Ca^{2+} with Eu^{3+} and Na^+, as suggested by the elemental composition analyses shown previously.

3.4. Extended X-ray absorption Fine Structure (EXAFS) study

The Mo K-edge EXAFS oscillations extracted from the XAS spectra and the Fourier transformed functions obtained for the undoped and Eu^{3+}-doped samples in the AMo (AMo-0, AMo-30 and AMo-50) and NaMo (NaMo-0, NaMo-30 and NaMo-50) systems are presented in **Figure 5a**. The fitting analysis of the main peak at around 1.35 Å in the FT function (without shift-phase correction), corresponding to the first Mo–O coordination shell yields the parameter values reported on **Table 2a**. It can be observed that, although the Mo-O distances remain at 1.78 Å within an estimated error of ±0.02 Å for all samples, the Debye-Waller factors notably increase from the parent samples (AMo-0 and NaMo-0) to the Eu-containing ones, the values being higher for the AMo samples. This result must be a consequence of changes in the type of cations in the neighboring *A* polyhedra, which are occupied by Ca^{2+}, Eu^{3+} and vacancies in the AMo samples and by Ca^{2+}, Eu^{3+} and Na^{+} in the NaMo ones. This different chemical surrounding consequently cause an increase in the static disorder in the Mo-O tetrahedra, more pronounced in the AMo-series, in agreement with the Raman observations.

On the other hand, the Eu L3-edge EXAFS oscillations extracted from the XAS spectra and the Fourier transformed functions obtained for the Eu-containing samples in the AMo (AMo-30 and AMo-50) and NaMo (AMo-30 and NaMo-50) systems are plotted in **Figure 5b**. The fitting analysis of the main peak at around 1.93 Å in the FT function (without shift-phase correction), corresponding to the first Eu–O coordination shell, yields ~8 neighbors atoms at 2.4 Å for all AMo and NaMo samples at any Eu content (**Table 2b**). These data are in agreement with Eu^{3+} ions occupying the *Ca* crystallographic sites in the $CaMoO_4$ scheelite structure. The Eu-O distance derived from the fitting analysis is in the range 2.40 – 2.41 Å for all four samples, which is sensibly lower than the average Ca-O distance in the parent structure (2.46Å)[4], in agreement with the higher electronegativity and lower ionic radius of Eu^{3+} compared with Ca^{2+}.

In summary, the analysis of Mo and Eu EXAFS spectra reveal that a certain local disorder takes place in the MoO_4 tetrahedron when Eu is incorporated into the scheelite structure, although Mo-O distances do not change, at least within the error of the measurement. Meanwhile, the Eu EXAFS spectra reveal that the Ca polyhedron is shrunk as a consequence of Eu^{3+} occupying Ca sites.

3.5. Synchrotron Powder Diffraction (SPD)

In order to gain deeper insight on the crystallographic structure of the $Ca_{1-3x}Eu_{2x}\square_xMoO_4$ and $Ca_{1-2x}Eu_xNa_xMoO_4$ solid solutions, as well as to clarify the origin of the observed expansion of the unit cell when replacing smaller Eu^{3+} for bigger Ca^{2+}, high resolution synchrotron powder diffraction patterns were recorded on all compositions of both AMo and NaMo systems.

Rietveld refinements were performed firstly on the AMo samples using the tetragonal scheelite structure as a starting model (space group $I4_1/a$), with Ca^{2+}, Eu^{3+} and vacancies randomly distributed in the unique Ca site of the parent $CaMoO_4$ structure. Attending to the $Ca_{1-3x}Eu_{2x}\square_xMoO_4$ formula described above, established from elemental analyses and

Raman spectroscopy, the following constraints have been used during the refinement: *i)* the vacancy content corresponds to half of the Eu^{3+} content and *ii)* the Ca^{2+} content was constrained so that the Ca site is fully occupied by Ca^{2+}, Eu^{3+} and vacancies. On the other hand, the Rietveld refinements of the NaMo series were also performed using the tetragonal scheelite structure as the starting model, with Ca^{2+}, Eu^{3+} and Na^{+} randomly distributed on the unique Ca site of the parent structure. In this case, attending to the expected substitution mechanism ($Ca_{1-2x}Eu_xNa_xMoO_4$), the constraints used during the refinement process were: *i)* the Eu^{3+} content was equal to the Na^{+} content (electro neutrality constraint) and *ii)* the Ca site was considered as fully occupied with either Ca^{2+}, Eu^{3+} or Na^{+}. This way we could determine the Eu^{3+} content in each sample. The final refined synchrotron powder diffraction diagrams for the AMo-30 and NaMo-30 compositions are shown in **Figure 6**, as an example, while **Figures S1-S3** show the refined diagrams for the rest of compositions. The formula units derived from the site occupation factors obtained for Ca^{2+}, Eu^{3+} and Na^{+} in the Rietveld analyses are given in the last column of Table 1. Comparison of the last two columns of Table 1 reveals that the formula units obtained from the Rietveld refinements are very similar to those obtained from EDX analyses, which confirms the substitution mechanisms proposed above for both AMo and NaMo systems.

The structural parameters resulting from the Rietveld refinements are given in **Table 3**. **Figure 7a** shows that the unit cell volume increases approximately linearly with increasing Eu^{3+} content in both systems. The cell volume increase observed in the NaMo samples with increasing Eu^{3+} content could be partially explained by the substitution mechanism itself, where one Na^{+} ion (ionic radius in VIII coordination= 1.18 Å) compensates and exceeds the expected volume decrease produced by the substitution of 2 Ca^{2+} ions (1.12 Å) by one Eu^{3+} (1.066 Å). However, the increase in the AO_8 polyhedra volume caused by this size difference is not big enough to explain the observed cell volume increase in this system. An additional factor must be playing a role in determining the unit cell volume of the Eu-containing samples, which is especially necessary to explain the case of the AMo system, where no Na^{+} is present to compensate the small Eu^{3+} radius. The key factor to explain the cell volume increase in both systems could be found on the different electronegativity values of Eu^{3+} and Ca^{2+}, which could influence the MoO_4 polyhedra volume and, eventually, the unit cell volume. The higher electronegativity of Eu^{3+} compared to Ca^{2+} is expected to attract oxygen ions apart from Mo^{6+} leading to an increase of the Mo-O distance, thus increasing the MoO_4 tetrahedron volume and consequently increasing the unit cell volume. The structure refinement shows, in fact, a very slight increase in the Mo-O distance (global increase is inside the EXAFS error) (**Figure 7b**), more noticeable in the AMo system because of its higher Eu content. This slight increase in the Mo-O distance leads to an increase of 1.7% and 2.5% in the MoO_4 tetrahedron volumes in the NaMo and AMo systems, respectively, **(Table 3)**, that are sufficient to explain the observed 0.7% and 1.2% increase in unit cell volume observed in both series.

3.6. Luminescence properties

The excitation spectra of the samples in the AMo and NaMo systems, recorded while monitoring the characteristic Eu^{3+} emission at 614 nm, are shown in **Figures 8a and 8b**. All the spectra show the characteristic intra-*4f* transition lines of Eu^{3+} with maximum intensity at 395 nm ($^7F_0 \rightarrow {}^5L_6$) and 465 nm ($^7F_0 \rightarrow {}^5D_2$). A broad band can be observed in the 250-350 nm interval, which has been usually assigned to the charge transfer (CT) absorption in MoO_4^{2-} groups in which an oxygen *2p* electron goes into one of the empty Mo *4d* orbitals.[5,14,21,22] The presence of the CT band in the excitation spectra while monitoring the Eu^{3+} emission clearly indicates the existence of energy transfer from MoO_4^{2-} to Eu^{3+}. The CT band shows a clear asymmetry in the excitation spectra of the AMo samples, with maxima at 265 nm and 295 nm, which is less pronounced in the NaMo spectra. Lv et al.,[22] in their analysis of the excitation spectrum of 3%Eu^{3+}-doped $CaMoO_4$, also noticed that the CT band was asymmetric; the band was fitted with two Gaussian curves (with maxima at 270 nm and 300 nm) that were assigned to the $^1A_1 \rightarrow {}^1T_2$ and $^1A_1 \rightarrow {}^1T_1$ transitions of the MoO_4^{2-} ions, respectively. It is important to say that, although several authors have assigned this broad band to the Eu-O charge transfer band,[8,12] this assignation has been however discarded on the basis of the expected value (238 nm) for the Eu-O charge transfer energy estimated for scheelites from Jorgensen equation.[23]

The emission spectra of the samples in the AMo and NaMo systems, recorded under an excitation wavelength of 275 nm, are shown in **Figures 8c and 8d.** All spectra show the same set of sharp emission bands, which are attributed to the characteristic intra *4f* transitions of Eu^{3+} ions ($^5D_0 - {}^7F_J$ with J = 0, 1, 2, 3, 4). The $^5D_0 - {}^7F_1$ transition corresponds to the magnetic dipole transition, which is insensitive to the crystal field environment of the Eu^{3+} ions, while the electric dipole transition ($^5D_0 - {}^7F_2$) is hypersensitive to the site symmetry of the Eu^{3+} ions. If Eu^{3+} is located in a site without inversion symmetry, the $^5D_0 - {}^7F_2$ transition should be dominant. Conversely, the intensity of the $^5D_0 - {}^7F_1$ transition became strong.[24] It can be observed in the emission spectra of Figures 8c and 8d that the intensity of the $^5D_0 - {}^7F_1$ transition (at 591 nm) is significantly lower than that of the $^5D_0 - {}^7F_2$ transition (double peak at 611 nm and 614nm), indicating the absence of inversion symmetry at the Eu^{3+} sites. This is in agreement with the replacement of Eu^{3+} for Ca^{2+} ions in the scheelite $CaMoO_4$ crystal structure, which shows S_4 site symmetry (no inversion center) on the Ca sites. Although the symmetry around Eu^{3+} could be altered as a consequence of Ca vacancies or Na^+ in the AO_8 polyhedra, the fact that the intensity ratio $^5D_0 - {}^7F_2$/ $^5D_0 - {}^7F_1$ does not appreciably change with increasing Eu content indicates the absence of inversion center at the Eu sites. The enormous intensity ratio between both bands gives rise to a high color purity, which is a well-known characteristic of $CaMoO_4$:Eu^{3+} phosphors.[25] The emission intensity of all bands decreases with increasing Eu^{3+} content, suggesting the existence of concentration quenching at 10% Eu^{3+}-doping level.

This indicates that the formation of Ca vacancies does not

To gain more information on the influence of vacancies and Na^+-content on the luminescence properties, we carried out an analysis of the luminescence dynamics on the Eu-containing samples belonging to both AMo and NaMo series. The decay curves obtained for the $^5D_0 \rightarrow {}^7F_2$ Eu^{3+} transition (614 nm) (**Figures 9a and 9b**) could be fitted, in all samples, by the bi-exponential decay function:

$$I(t) = I_{01} \exp(-t/\tau_1) + I_{02} \exp(-t/\tau_2) \qquad (1)$$

where I(t) is the luminescence intensity, t is the time after excitation and τ_i (i = 1, 2) is the decay time of the i-component with intensity I_{0i}. The fitting parameters are shown in **Table 4**, along with the average lifetime values, $<\tau>$, calculated as:

$$\langle \tau \rangle = \frac{\int_{t_0}^{t_f} tI(t)dt}{\int_{t_0}^{t_f} I(t)dt} = \left(\tau_1^2 I_1 + \tau_2^2 I_2\right) / \left(\tau_1 I_1 + \tau_2 I_2\right) \qquad (2)$$

where t_f represents the time required for the luminescence signal to reach the background. The bi-exponential decay observed for all six substituted samples is in agreement with previous reports on this phosphor[11,14] and has been assigned to Eu^{3+} ions on the particle surface (short lifetime) and in the particle bulk (long lifetime). While the short lifetime values stay practically constant with increasing Eu content in both series, the long lifetime values considerably decrease with increasing Eu content, as expected from concentration quenching effects. **Figure 9c** represents the average lifetime as a function of the experimental Eu^{3+} content for all samples in the AMo and NaMo series. It can be observed that the average lifetime values decrease with increasing Eu^{3+} content following a linear dependence that fits all six samples. This result suggests that the average lifetime is not affected by the substitution mechanism itself, i.e., presence of vacancies or Na^+ in the crystal structure, but it seems to exclusively depend on the Eu^{3+} concentration of the sample.

In order to confirm this result, we have further analyze the influence of vacancies and Na^+ on the luminescence efficiency of the samples using quantum yield (QY) measurements (**Table 5 and Figure 10**), which certainly inform on phosphors efficiency. QY values wer obtained for both the AMo and NaMo series under excitation at the wavelength corresponding to the charge transfer band (295 nm). The QY values obtained for AMo-10 and NaMo-10 (both containing approximately the same experimental mol% Eu^{3+}) were very similar to one another (58% and 57%, respectively). This result, together with the structural study reported in this paper indicates that the luminescence efficiency does not increase with the presence of Na^+ in the crystalline structure, contrary to previous observations, which do not present QY values.[5,17] This result is further supported by the fact that the evolution of the QY values *versus* Eu content (Figure 10) fits to a unique linear behavior for samples in both AMo and NaMo series, indicating that the luminescence behavior of both series is similar. We want to note that the decrease in the

QY values can be explained on the basis of the well-known concentration quenching effect, already inferred from the lifetime values. This is, to the best of our knowledge, the first report on QY values in Eu:$CaMoO_4$ and Eu,Na:$CaMoO_4$ phosphors.

4. CONCLUSIONS

The substitution mechanism in Eu^{3+}:$CaMoO_4$ and Eu^{3+},Na^{+}:$CaMoO_4$ phosphors is different, with Ca site vacancies forming in the former, thus leading to $Ca_{1-3x}Eu_{2x}\square_xMoO_4$ compositions, while the latter formed $Ca_{1-2x}Eu_xNa_xMoO_4$ compositions to reach charge balance. The cell volume increase observed in the NaMo samples with increasing Eu^{3+} content, can be partially explained by the bigger Na^{+} ionic radius (1.18 Å) which compensates and slightly exceeds the expected volume decrease produced by the substitution of Ca^{2+} (1.12 Å) by Eu^{3+} (1.066 Å). However, the increase in the AO_8 polyhedra volume caused by this size difference is not sufficient as to explain the observed cell volume increase in this system. We propose that the key factor explaining the unit cell volume increase with increasing Eu content in both systems is the higher electronegativity of Eu^{3+} *vs.* Ca^{2+}. Eu^{3+} attracts oxygen ions apart from Mo^{6+} leading to an increase of the Mo-O distance, which increases the MoO_4 tetrahedron volume and consequently the unit cell volume. Finally, it was shown that the luminescence properties, i.e. lifetime values and quantum yields, do not depend on the presence of monovalent ions in the crystal structure, but, exclusively, on the Eu^{3+} content of the phosphors, independently on whether they belong to the AMo or to the NaMo series.

SUPPLEMENTARY INFORMATION

Synchrotron powder diffraction patterns (experimental, fitted and difference curves) of AMo and NaMo samples with different Eu^{3+} contents are given in Figures S1 to S3.

ELECTRONIC SUPPLEMENTARY INFORMATION

Crystallographic information files. Further details of the crystal structure investigation(s) may be obtained from the Fachinformationszentrum Karlsruhe, 76344 Eggenstein-Leopoldshafen (Germany), on quoting the depository numbers CSD 1866205 (AMo30), CSD 1866206 (NaMo10), CSD 1866207 (NaMo30), CSD 1866208 (NaMo0), CSD 1866209 (AMo0), CSD 1866210 (AMo10), CSD 1866211 (NaMo50), CSD 1866212 (AMo50).

CONFLICTS OF INTEREST

There are no conflicts of interest to declare.

ACKOWLEDGEMENTS

This work was supported by CSIC projects (PIC2016FR1 and PIE201460E005) and the European Research Council (ERC) under the European Union's Horizon 2020 research and innovation programme (NANOPHOM, grant agreement n° 715832).

REFERENCES

1 V. B. Mikhailik, H. Kraus, *J. Appl. Phys.*, 2005, **97**, 083523.
2 S. S. Hosseinpour-Mashkani, S. S. Hosseinpour-Mashkani, A. Sobhani-Nasab., *J. Mater. Sci. Mater. Electron,* 2016, **27**, 4351.
3 G. S. R. Raju, E. Pavitra, Y. H. Ko, J. S. Yu., *J. Mater. Chem.*, 2012, **22**, 15562.
4 G. Wandahl, A. N. Christensen, *Acta Chem. Scand., Ser. A*, 1987, **41**, 358.
5 J. Liu, H. Lian, C. Shi, *Opt. Mater.,* 2007, **29**, 1591.
6 H. Wu, Y. Hu, W. Zhang, F. Kang, N. Li, G. Ju, *J. Sol-Gel Sci. Technol.,* 2012, **62**, 227.
7 A. Khanna, P. S. Dutta, *J. Solid State Chem.,* 2013, **198**, 93.
8 S. K. Gupta, M. Sahu, P. S. Ghosh, D. Tyagi, M. K. Saxena, R. M. Kadam, *Dalton Trans.*, 2015, **44**, 18957.
9 R. Saraf, C. Shivakumara, N. Dhananjaya, S. Behera, H. Nagabhushana, *J. Mater. Sci.,* 2015, **50**, 287.
10 X. Liu, L. Li, H. M. Noh, J. H. Jeong, K. Jang, D. S. Shin, *RSC Adv.*, 2015, **5**, 9441.
11 M. Laguna, N. O. Nuñez, A. I. Becerro, M. Ocaña, *CrystEngComm,* 2017, **19**, 1590.
12 S. Yu, Z. Lin, L. Zhang, G. Wang, *Cryst. Growth Des.*, 2007, **7**, 2397.
13 A. K. Parchur, R. S. Ningthoujam, *Dalton Trans.*, 2011, **40**, 7590.
14 Z. Hou, R. Chai, M. Zhang, C. Zhang, P. Chong, Z. Xu, G. Li, J. Lin, *Langmuir,* 2009, **25**, 12340.
15 C. Hazra, T. Samanta, A. V. Asaithambi, V. Mahalingam, *Dalton Trans.,* 2014, **43**, 6623.
16 C. Zhao, Q.Y. Meng, W.J. Sun, *Acta Phys. Sin.*, 2015, **64**, 107803.
17 Z. H. Zhang, Q. Huang, X. Zhao, Z. L. Huang, *Phys. Status Solidi A*, 2009, **206**, 2839.
18 Y. Su, L. Li, G. Li, *Chem. Mater.*, 2008, **20**, 6060.
19 S. P. Culver, F. A. Rabuffetti, S. Zhou, M. Mecklenburg, Y. Song, B. C. Melot, R. L. Brutchey, *Chem. Mater.*, 2013, **25**, 4129.
20 P. Godlewska, E. Tomaszewicz, L. Macalik, J. Hanuza, M. Ptak, P. E. Tomaszewski, M. Maczka, P. Ropuszynska-Robak, *Mater. Chem. Phys.,* 2013, **139**, 890.
21 K. G. Sharma, T. P. Singh, N. R. Singh, *J. Alloys Compd.,* 2014, **602**, 275.
22 L. Lv, J. Wang, W. Wang, L. Han, *J. Alloys Compd.,* 2015, **635**, 25.
23 C. K. Jørgensen, Electron Transfer Spectra; John Wiley & Sons, Inc.: New York, 1970; pp 101-158
24 G. S. Ofelt, *J. Chem. Phys.*, 1962, **37**, 511.
25 Y. Hua, W. Zhuang, H. Ye, D. Wang, S. Zhang, X. Huang, *J. Alloys Compd.,* 2005, **390**, 226.

Table 1: EDX elemental analyses of the undoped and Eu-doped $CaMoO_4$ samples in the AMo and NaMo systems. The values have been normalized to Molybdenum molar content. Formula units derived from the elemental analyses as well as from Rietveld analyses of the synchrotron powder diffraction data are given in the last two columns. □ represents cationic vacancies.

Sample name	Mo	Ca	Eu	Na	Formula unit deduced from EDS	Formula unit deduced from Rietveld*
AMo-0	1.00	1.01	0.0	0.00	$Ca_{1.01}MoO_4$	$CaMoO_4$
AMo-10	1.00	0.90	0.09	0.00	$Ca_{0.90}Eu_{0.09}□_{0.01}MoO_4$	$Ca_{0.84}Eu_{0.11}□_{0.05}MoO_4$
AMo-30	1.00	0.65	0.24	0.00	$Ca_{0.65}Eu_{0.24}□_{0.11}MoO_4$	$Ca_{0.58}Eu_{0.28}□_{0.14}MoO_4$
AMo-50	1.00	0.44	0.36	0.00	$Ca_{0.44}Eu_{0.36}□_{0.20}MoO_4$	$Ca_{0.40}Eu_{0.40}□_{0.20}MoO_4$
NaMo-0	1.00	1.04	0.0	0.01	$Ca_{1.04}Na_{0.01}MoO_4$	$CaMoO_4$
NaMo-10	1.00	0.87	0.10	0.08	$Ca_{0.87}Eu_{0.10}Na_{0.08}MoO_4$	$Ca_{0.80}Eu_{0.10}Na_{0.10}MoO_4$
NaMo-30	1.00	0.60	0.18	0.21	$Ca_{0.60}Eu_{0.18}Na_{0.21}MoO_4$	$Ca_{0.56}Eu_{0.22}Na_{0.22}MoO_4$
NaMo-50	1.00	0.38	0.29	0.29	$Ca_{0.38}Eu_{0.29}Na_{0.29}MoO_4$	$Ca_{0.35}Eu_{0.33}Na_{0.33}MoO_4$

*During Rietveld refinement, the Mo site was considered as fully occupied by Mo (the content was first refined to check that it was almost 1). Then compositional constraints were used: Ca+Eu + □ = 1. Eu=2 x □. For NaMo samples, we used Ca+Eu+Na=1 and Eu=Na (and still Mo=1). Mo was fixed to 1.

Table 2a: Structural parameters for Mo obtained by fitting analysis of the EXAFS spectra

Sample name	Mo-O (Å)	C.N.	D-W (A^2x10^{-3})	ΔE_0 (eV)
AMo-0	1.78	4.0	0.82	2.76
AMo-30	1.78	4.0	1.46	3.05
AMo-50	1.78	4.0	1.51	2.94
NaMo-0	1.78	3.9	0.57	2.65
NaMo-30	1.78	3.9	1.02	2.77
NaMo-50	1.78	3.5	1.03	3.37

C.N.: Coordination number; D-W.: Debye-Waller factor
Estimated errors: Interatomic Distance, < ±0.02 Å; C.N. < ±10%.

Table 2b: Structural parameters for Eu obtained by fitting analysis of the EXAFS spectra

Sample name	Eu-O (Å)	C.N.	D-W (A^2x10^{-3})	ΔE_0 (eV)
AMo-30	2.41	7.3	4.43	4.11
AMo-50	2.40	7.8	7.06	3.56
NaMo-30	2.41	8.3	5.95	3.81
NaMo-50	2.40	7.5	5.21	3.81
Eu_2O_3	2.33	6.0	8.00	4.40

C.N.: Coordination number; D-W.: Debye-Waller factor
Estimated errors: Interatomic Distance, < ±0.02 Å; C.N. < ±10%.

Table 3: Unit cell parameters, unit cell volume and interatomic distances determined for undoped and Eu-doped $CaMoO_4$ samples, in the AMo and NaMo systems, from Rietveld refinement of the Synchrotron Powder Diffraction patterns.

Sample name	a cell (Å)	c cell (Å)	Volume ($Å^3$)	(*A*-O)1 distance (Å)	(*A*-O)2 distance (Å)	Mo-O distance (Å)	MoO_4 volume ($Å^3$)
AMo							
0	5.22662(1)	11.4339(1)	312.345(1)	2.461(1)	2.440(1)	1.789(1)	2.922
10	5.23178(1)	11.4365(1)	313.032(1)	2.465(1)	2.441(1)	1.789(1)	2.924
30	5.23772(1)	11.4567(1)	314.299(1)	2.459(2)	2.446(2)	1.797(2)	2.956
50	5.23794(1)	11.5184(1)	316.018(1)	2.449(2)	2.442(2)	1.808(2)	2.996
NaMo							
0	5.22616(1)	11.4366(1)	312.346(1)	2.462(1)	2.440(1)	1.788(1)	2.916
10	5.23194(1)	11.4366(1)	313.059(1)	2.467(1)	2.443(1)	1.787(1)	2.911
30	5.23692(1)	11.4426(1)	313.817(1)	2.465(1)	2.444(1)	1.791(1)	2.929
50	5.24149(1)	11.4482(1)	314.518(1)	2.471(1)	2.438(1)	1.798(2)	2.967

Table 4: Lifetime values (τ_1, τ_2), corresponding weighting factor (I_{01}, I_{02}) and average decay time ($<\tau>$) for the Eu-doped $CaMoO_4$ samples (AMo and NaMo systems) obtained for the $^5D_0$–$^7F_2$ transition of Eu^{3+} (614 nm) after pulsed excitation with λ_{exc} 275 nm.

Sample name	τ_1 (μs)	I_{01} (%)	τ_2 (μs)	I_{02} (%)	$<\tau>$ (μs)
AMo-10	495	96	1219	4	558
AMo-30	433	92	733	8	473
AMo-50	368	77	239	23	347
NaMo-10	495	98	1397	2	532
NaMo-30	448	95	766	5	472
NaMo-50	386	74	515	26	427

Table 5: Quantum yield values of the samples in the AMo and NaMo series.

Nominal mol %Eu^{3+}	AMo	NaMo
10	58 %	57 %
30	40 %	53 %
50	20 %	36 %

Figure 1

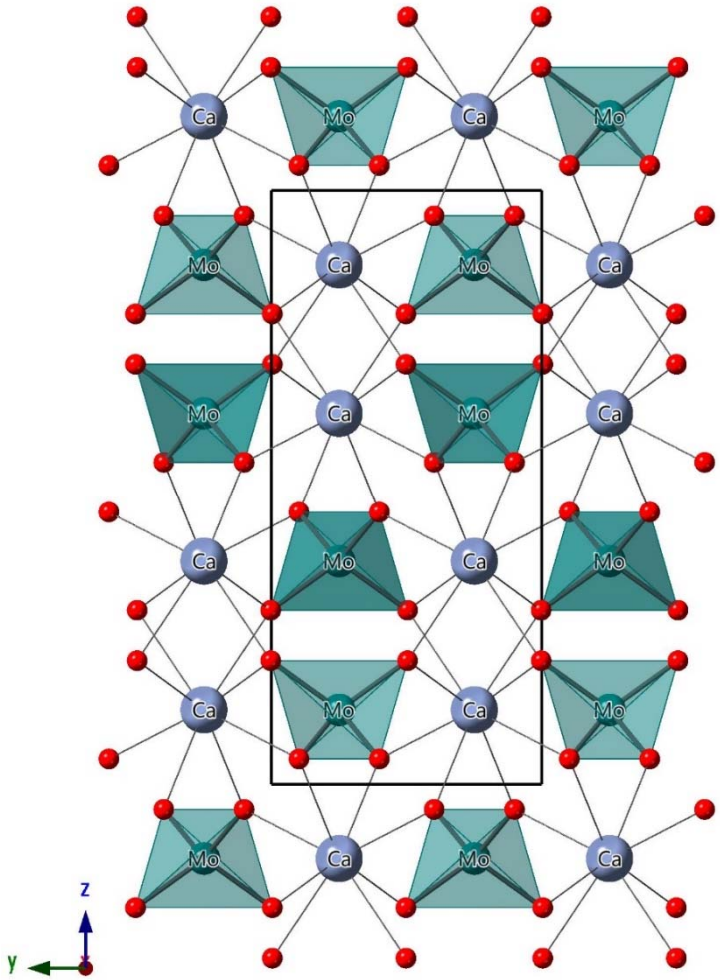

Figure 1: Schematic plot for the $CaMoO_4$ scheelite structure showing MoO_4 tetrahedra sharing all corners with Ca in eight-fold coordination. Red spheres denote oxygen.

Figure 2

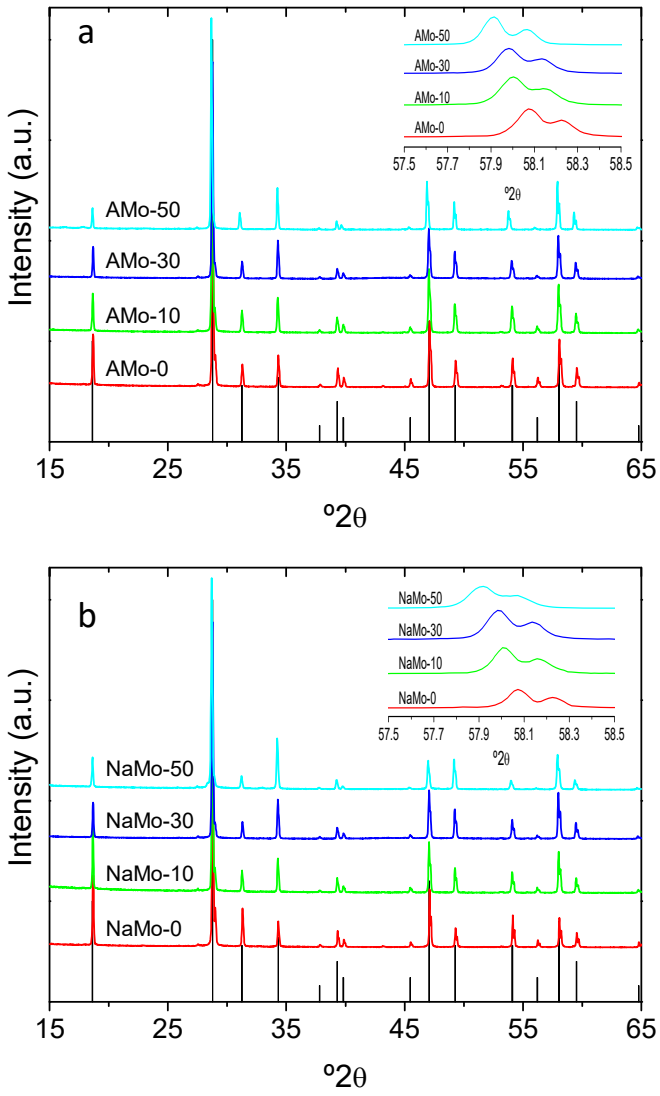

Figure 2: Laboratory XRD patterns of the undoped and Eu-doped $CaMoO_4$ samples synthesized from *a)* ammonium molybdate (AMo series) and *b)* sodium molybdate (NaMo series). The insets are magnifications of the 57.5 – 58.5 º2Θ region to better observe the reflections shift. Reflections of PDF 00-029-0351, corresponding to $CaMoO_4$ scheelite structure, are shown at the bottom of each figure.

Figure 3

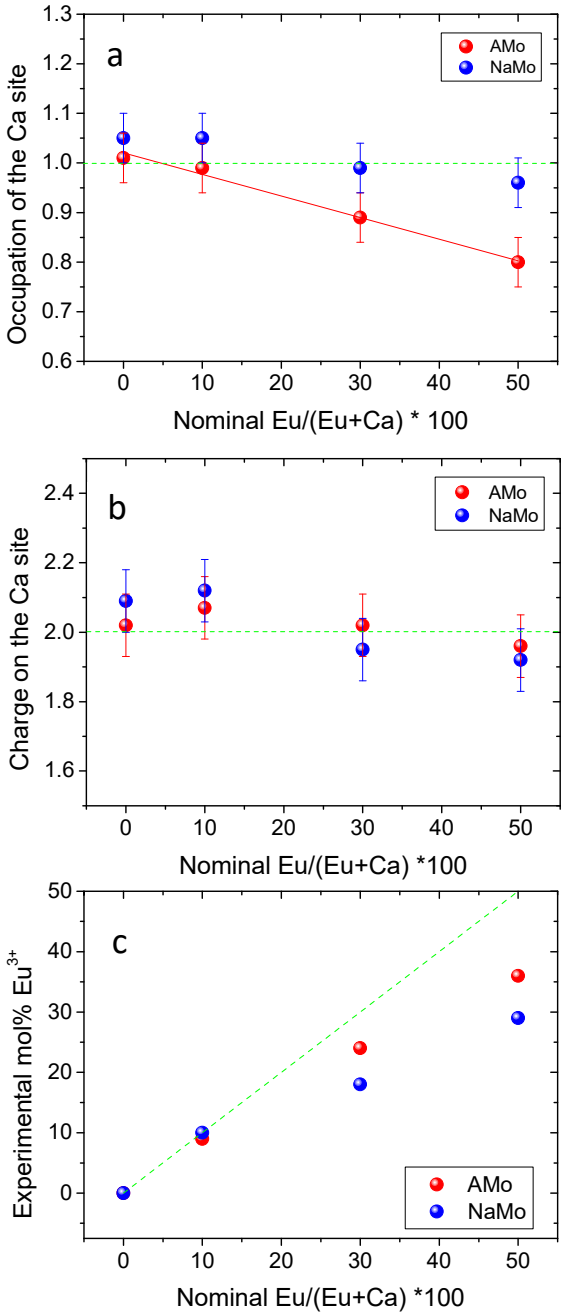

Figure 3: EDS data of the undoped and Eu-doped $CaMoO_4$ samples in the AMo and NaMo systems plotted as: *a)* Occupation of the *A* site *versus* nominal Eu^{3+} content. The occupation of the *A* site was calculated as the sum of Ca and Eu contents in AMo and Ca, Eu and Na contents in NaMo. *b)* Charge value on the Ca site *versus* nominal Eu^{3+} content. Charge values were calculated after weighted average of charges in Ca^{2+} and Eu^{3+} in AMo and of Ca^{2+}, Eu^{3+} and Na^{+} charge in NaMo. *c)* Experimental mol% of Eu^{3+} *versus* nominal Eu^{3+} content.

Figure 4

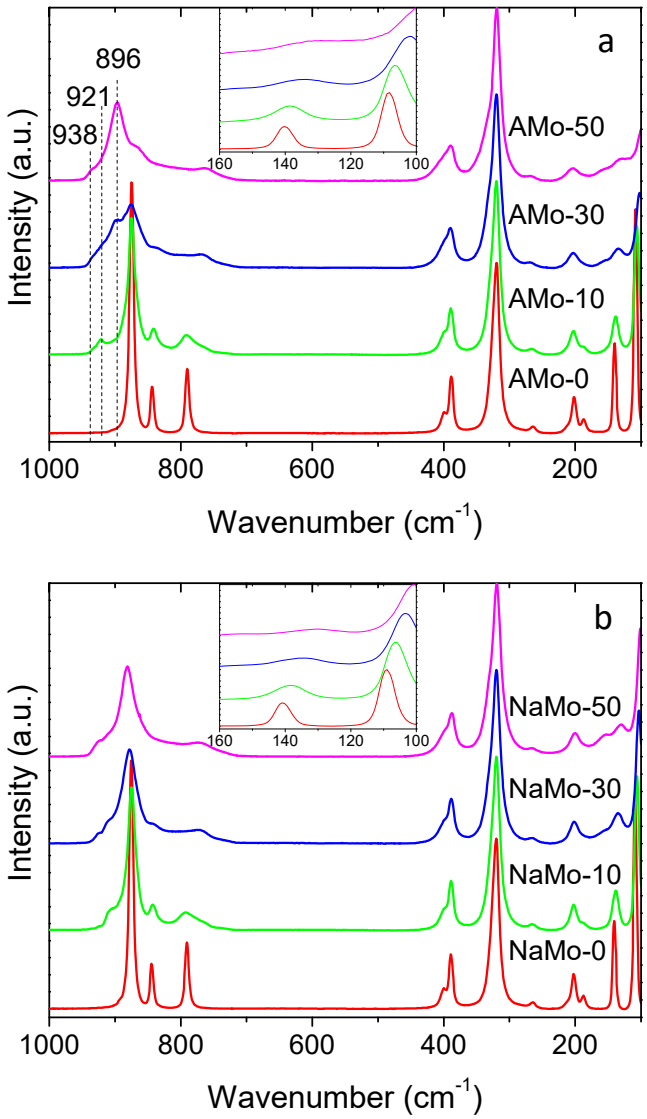

Figure 4: Raman spectra of the undoped and Eu-doped $CaMoO_4$ samples in the AMo *(a)* and NaMo *(b)* series. The insets are magnifications of the 160 -100 cm^{-1} region for a better observation of bands shift.

Figure 5

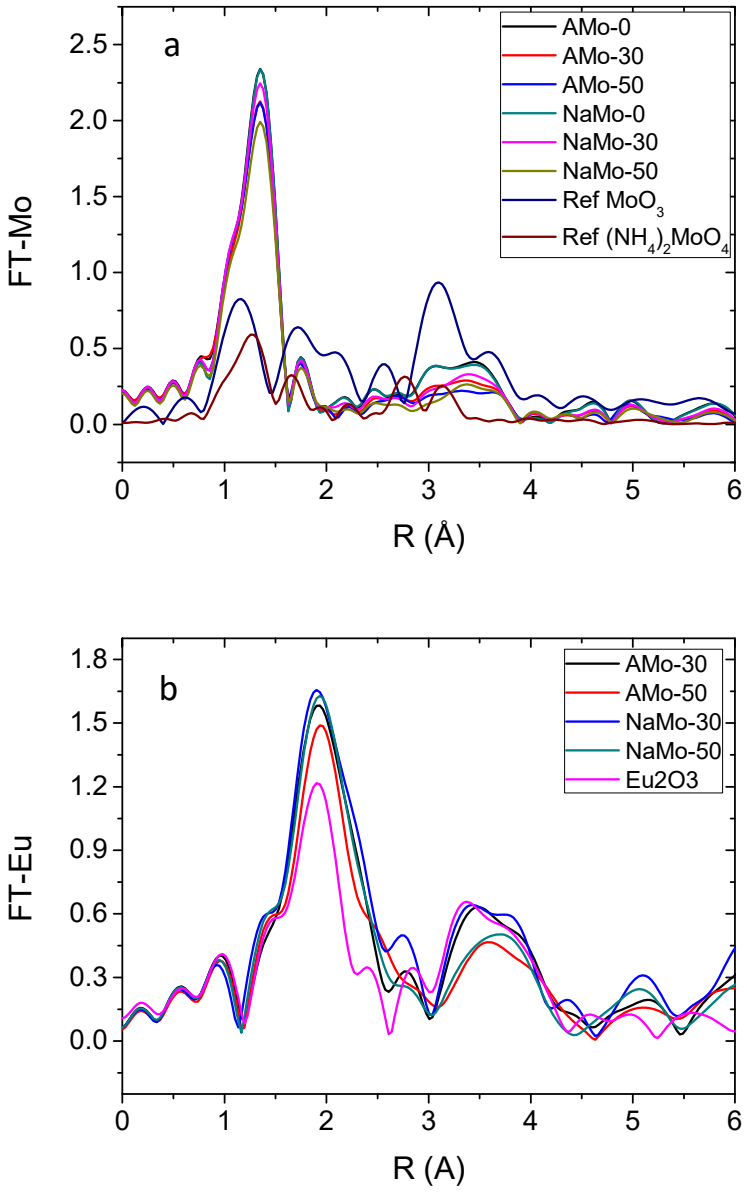

Figure 5: Fourier Transforms of Mo (top) and Eu (bottom) EXAFS oscillations of samples in the AMo and NaMo systems.

Figure 6

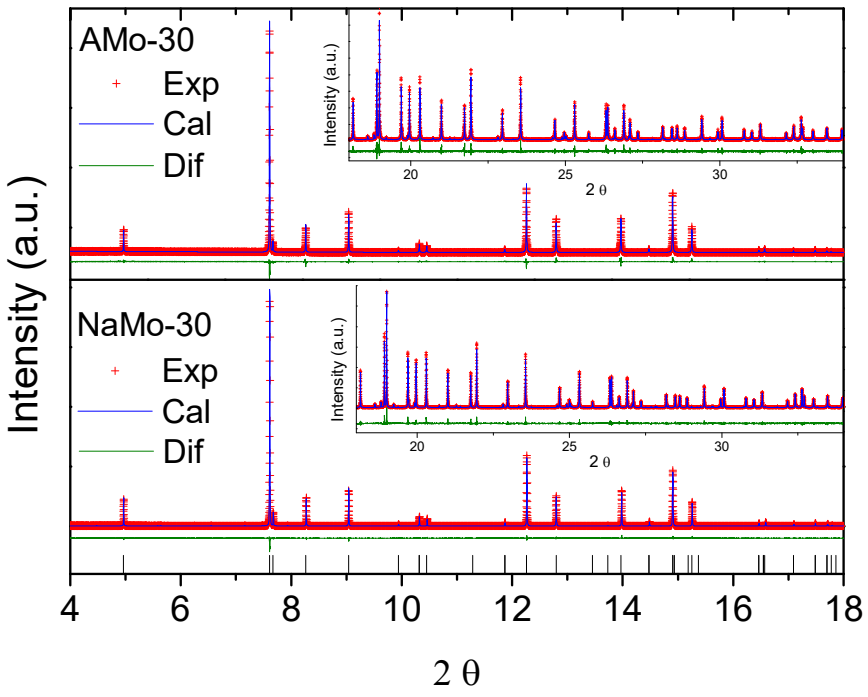

Figure 6: Experimental (crosses), fitted (blue solid line) and difference curve (green solid line) of the SPD diagrams obtained for AMo-30 and NaMo-30 samples.

Figure 7

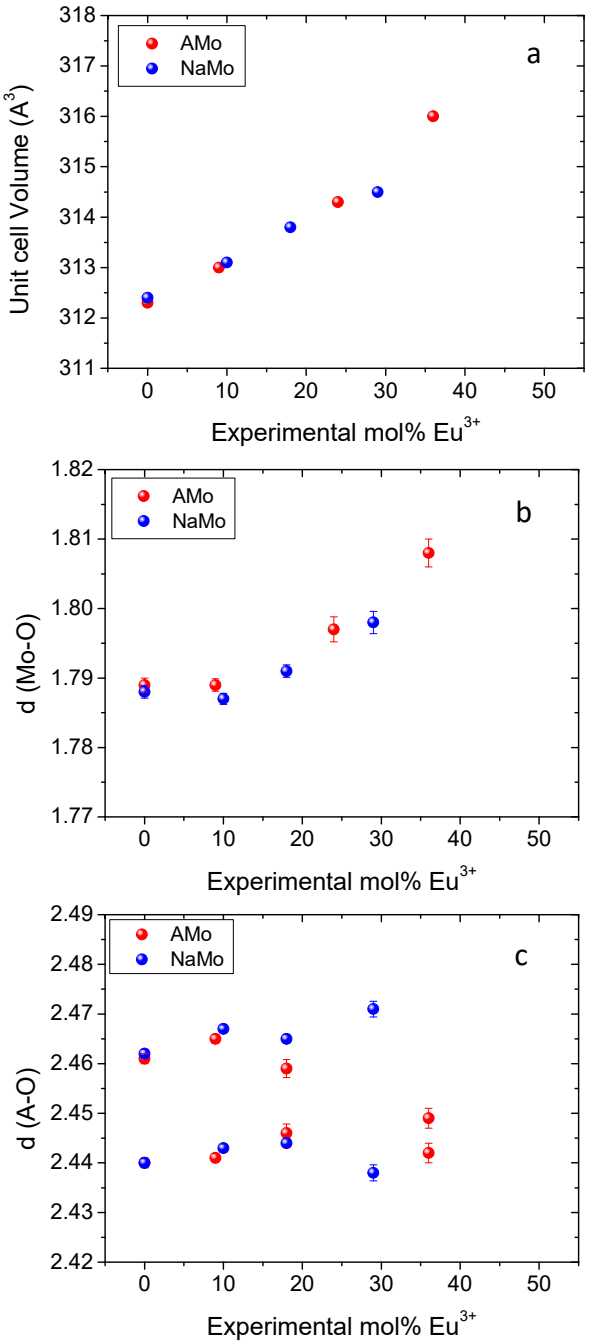

Figure 7: a) Unit cell volume, b) Mo-O distance and c) Ca-O distance (Ca= Ca, Eu, and Na, the latter only in NaMo samples), obtained from Rietveld refinement of Synchrotron Powder Diffraction data, *versus* the experimental Eu^{3+} content for undoped and Eu-doped $CaMoO_4$ samples in the AMo and NaMo systems.

Figure 8

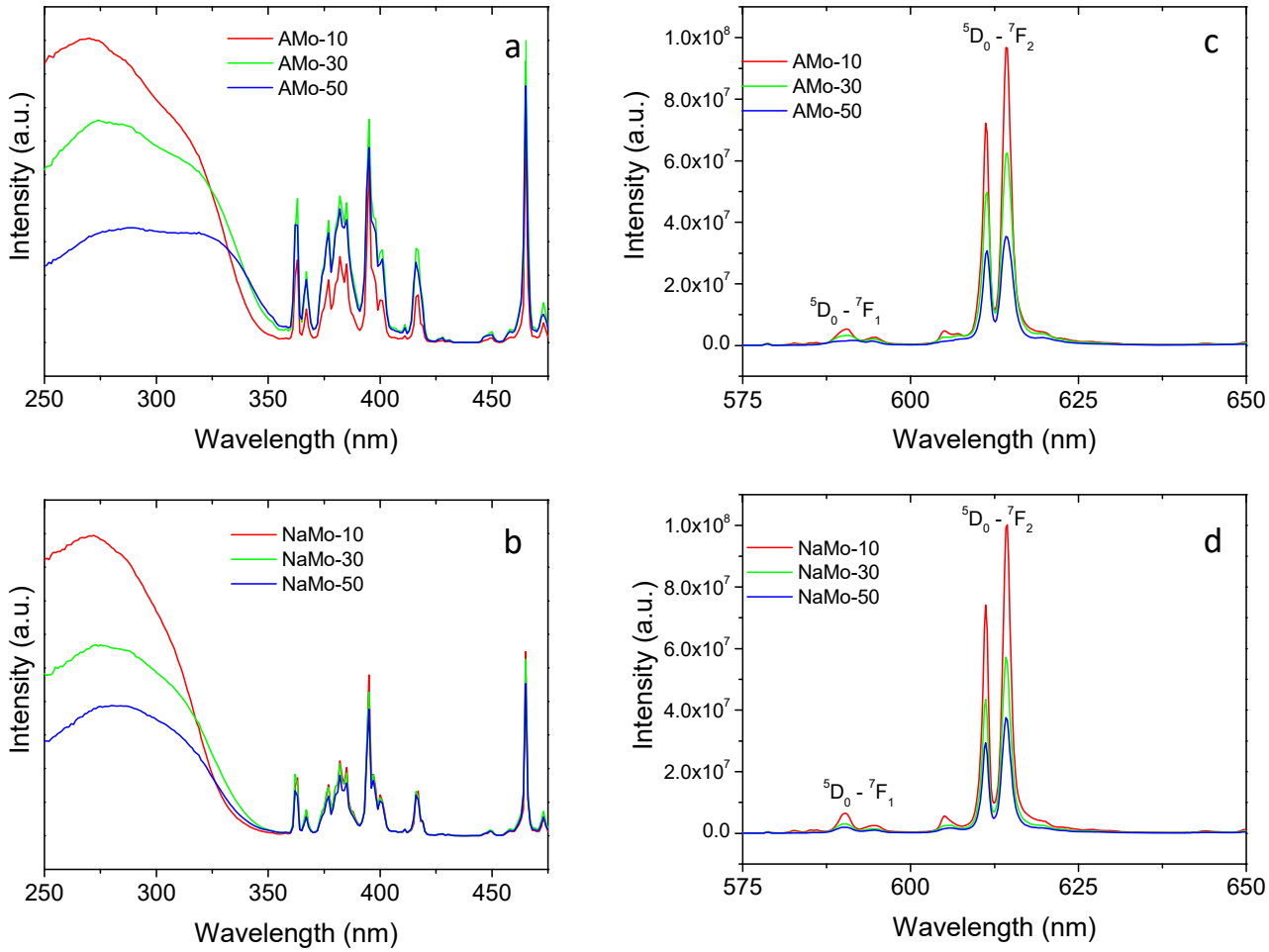

Figure 8: *a* and *b)* Excitation spectra (λ_{em}= 614 nm) recorded on the Eu-doped $CaMoO_4$ samples in the AMo and NaMo, respectively. *c and d)* Emission spectra (λ_{ex}= 275 nm) recorded on the on the Eu-doped $CaMoO_4$ samples in the AMo and NaMo, respectively.

Figure 9

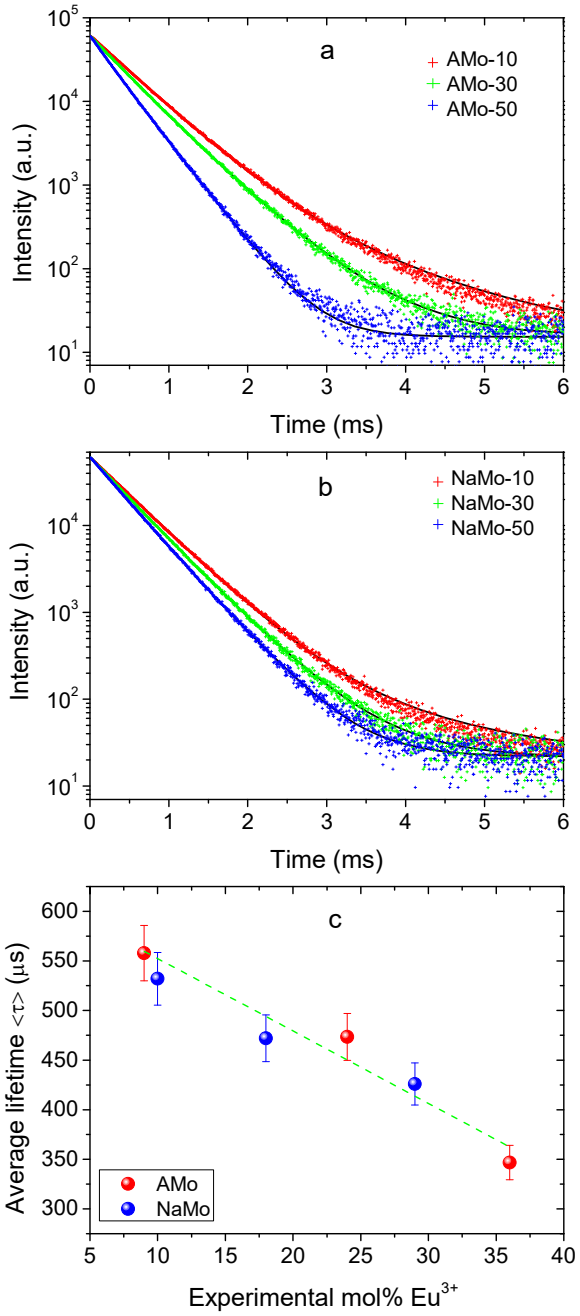

Figure 9: *a* and *b)* Temporal evolution of the Eu^{3+} $^5D_0$ → $^7F_2$ (614 nm) photoluminescence for the Eu-doped $CaMoO_4$ samples in the AMo and NaMo systems, respectively. *c)* Average lifetime calculated from the right hand-side term of Eq. (1), using the corresponding fitting parameters given in Table 4, *versus* the experimental Eu^{3+} content for the AMo and NaMo samples. The dashed line is a guide to the eye.

Figure 10

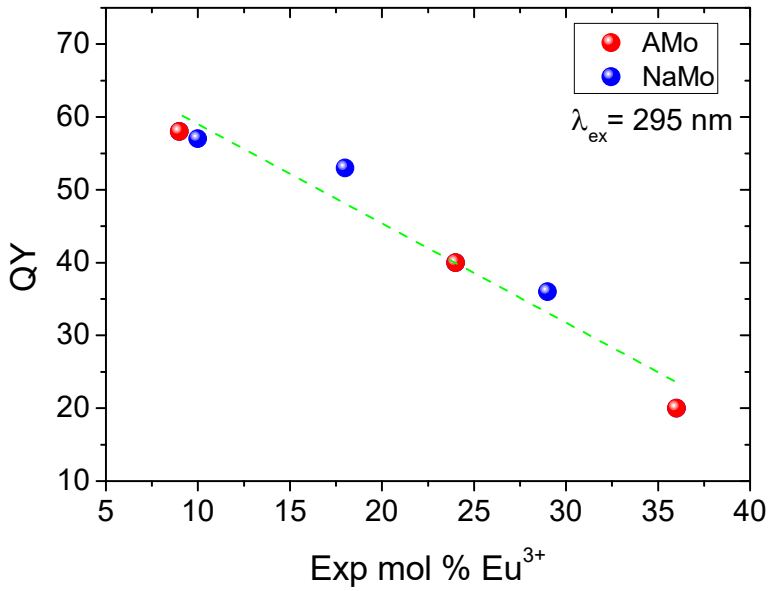

Figure 10: Quantum yield values of the samples in the AMo and NaMo series, recorded under excitation at 295 nm, versus the experimental mol % Eu^{3+}. The dashed line is a guide to the eye.